

RSONet: Region-guided Selective Optimization Network for RGB-T Salient Object Detection

Bin Wan, Runmin Cong, Xiaofei Zhou, Hao Fang, Chengtao Lv, and Sam Kwong, *Fellow, IEEE*

Abstract—This paper focuses on the inconsistency in salient regions between RGB and thermal images. To address this issue, we propose the Region-guided Selective Optimization Network for RGB-T Salient Object Detection, which consists of the region guidance stage and saliency generation stage. In the region guidance stage, three parallel branches with same encoder-decoder structure equipped with the context interaction (CI) module and spatial-aware fusion (SF) module are designed to generate the guidance maps which are leveraged to calculate similarity scores. Then, in the saliency generation stage, the selective optimization (SO) module fuses RGB and thermal features based on the previously obtained similarity values to mitigate the impact of inconsistent distribution of salient targets between the two modalities. After that, to generate high-quality detection result, the dense detail enhancement (DDE) module which adopts the multiple dense connections and visual state space blocks is applied to low-level features for optimizing the detail information. In addition, the mutual interaction semantic (MIS) module is placed in the high-level features to dig the location cues by the mutual fusion strategy. We conduct extensive experiments on the RGB-T dataset, and the results demonstrate that the proposed RSONet achieves competitive performance against 27 state-of-the-art SOD methods.

Index Terms—RGB-T salient object detection, region-guided, selective optimization.

I. INTRODUCTION

SALIENT object detection (SOD) [1]–[8], as a prominent computer vision task, aims to mimic the human perceptual ability to identify the main object within a scene. Unlike traditional object detection tasks that require bounding boxes around the object area, SOD emphasizes the target area at the pixel level. Consequently, it can serve as a pre-processing technique for various scene applications, such as semantic segmentation [9]–[17], image enhancement [18]–[22], person re-identification [23], [24], and image understanding [25], [26]. In recent years, the rapid advancement of deep learning technology [27]–[29] has significantly improved salient object detection. However, when dealing with challenging scenes

such as complex backgrounds, low contrast, and unclear boundaries, RGB image-based SOD methods exhibit sub-optimal performance. Therefore, it is necessary to incorporate additional information to compensate for the limitations of RGB images. At the early stage, benefiting from the practicality of various depth information acquisition devices which provide more shape structure and boundary information, depth cues are introduced to the SOD tasks, generating the RGB-D salient object detection [30]–[33] and enhancing the detection performance to a certain extent. Nevertheless, when the object and background regions are adjacent, accurately distinguishing the object in the depth map becomes extremely challenging, thereby undermining the utility of depth information. To address this issue, researchers have attempted to introduce an additional source of information (thermal data), resulting in the development of RGB-T salient object detection. For example, in [34], Ma *et al.* proposed a novel modal complementary fusion network which designs the modal reweight module and spatial complementary fusion module to mitigate the impact of low-quality images. In [35], Lv *et al.* proposed a transformer-based cross-modal integration network where the cross-modal feature fusion module and interaction-based feature decoding block are leveraged to explore the complementarity of two-modal information. In [36], Zhou *et al.* explored RGB-T salient object detection from the frequency perspective, and proposed the frequency-aware multi-spectral feature aggregation module and HF-guided signed distance map prediction module. Although thermal information is not affected by spatial position, it may still be influenced by other factors such as environmental conditions and material properties, resulting in an excessive information discrepancy between the two modalities. As shown in Fig. 1, we can see that the object area in the first row is almost indistinguishable from the background area in the thermal map. In contrast, the brick in the second row exhibits similar characteristics to the background area in the RGB image. Most existing methods fuse the two modalities using operations such as addition, multiplication, concatenation, or various attention mechanisms. However, these fusion strategies inherently assume equal importance between the modalities, which can lead to the introduction of substantial irrelevant noise when significant information disparities exist between them, thereby impairing the accurate segmentation of object regions.

To address the issues mentioned above, we propose a Region-guided Selective Optimization Network (RSONet) for RGB-T Salient Object Detection which consists of region guidance and saliency generation phases to mitigate the negative impact stemming from the uneven distribution of the

This work was supported in part by the the National Natural Science Foundation of China under Grant 62471278, Grant 62271180, and in part by the Research Grants Council of the Hong Kong Special Administrative Region, China under Grant STG5/E-103/24-R. (*Corresponding author: Runmin Cong*).

Bin Wan, Runmin Cong and Hao Fang are with the School of Control Science and Engineering, Shandong University, Jinan 250061, China, and also with the Key Laboratory of Machine Intelligence and System Control, Ministry of Education, Jinan 250061, China. (E-mail: wanbinxueshu@icloud.com; rmcong@sdu.edu.cn; fanghaook@mail.sdu.edu.cn).

Xiaofei Zhou is with School of Automation, Hangzhou Dianzi University, Hangzhou 310018, China (E-mail: zxforchid@outlook.com).

Chengtao Lv is with School of information engineering, Huzhou University, Huzhou 313000, China (E-mail: chengtaolv@outlook.com).

Sam Kwong is with the School of Data Science, Lingnan University, Tuen Mun, Hong Kong (E-mail: samkwong@ln.edu.hk).

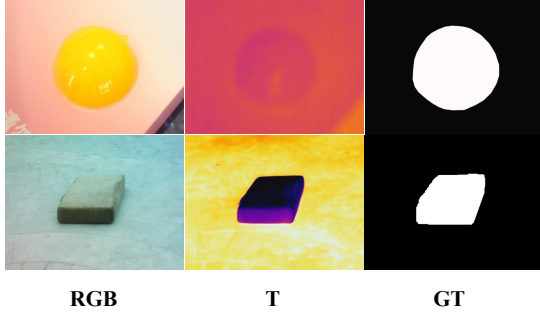


Fig. 1: Examples of RGB-T challenge scenarios.

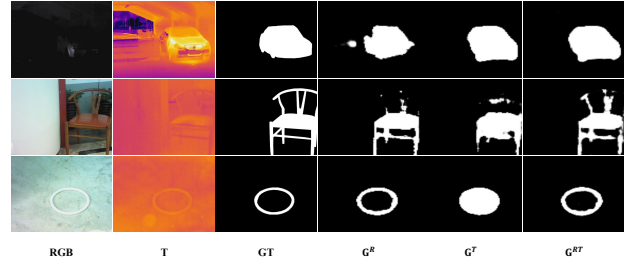


Fig. 3: Illustration of the guidance map.

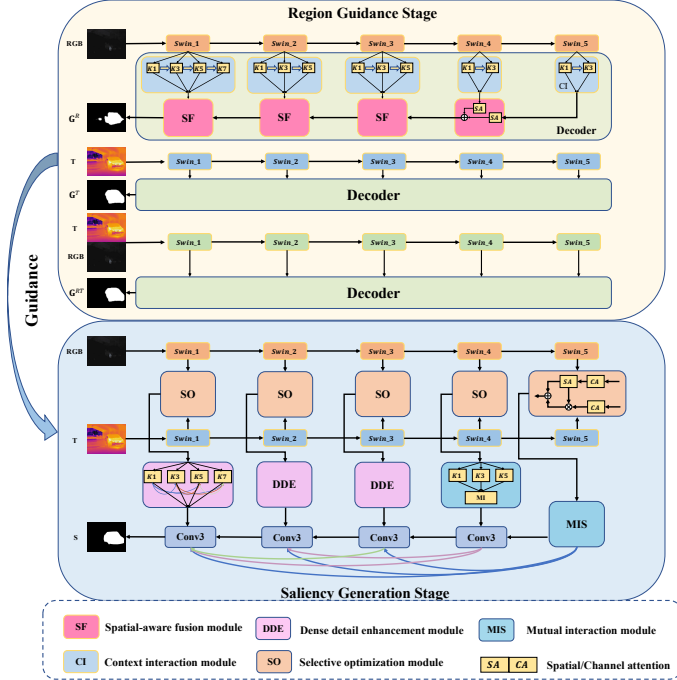


Fig. 2: Illustration of the RSONet.

saliency regions across the two modalities and yield high-quality saliency map.

A. Region Guidance

To address the issue of inconsistent salient regions, we first design the region guidance phase to ensure that the modality with more accurate salient information takes the lead during the subsequent bimodal fusion stage. As shown in Fig. 2, the region guidance phase contains three parallel branches which adopt the same encoder-decoder structure, where the inputs for the first two branches (*i.e.*, R and T) are the RGB image and the thermal map, respectively, while the sum of the RGB image and the thermal map serves as the input for the third branch (*i.e.*, RT). Firstly, SwinTransformer [37] as the backbone network is adopted to extract multi-level features from the input. To further excavate the saliency region, we design the context interaction (CI) module, which employs convolutions with varying kernel sizes for different levels of features, enabling the capture of contextual information of the object area across different receptive fields. Then,

in order to drive the generation of saliency guidance maps for three branches, the spatial-aware fusion (SF) module is proposed to fuse features yielded from the CI module layer by layer, where the spatial attention mechanism is employed to encourage the model to focus on salient object areas. Considering that the input of branch RT is the sum of the RGB and thermal images, the resulting guidance map G^{RT} contains richer object information. Therefore, we compare the similarity between the guidance maps of branch R and branch T with the result of branch RT, respectively, to determine which modality should dominate during the modality fusion stage for saliency generation.

B. Saliency Generation

After the region guidance stage, the modality with the most accurate salient information is selected, which dominates the bimodal feature fusion process in the subsequent selective optimization (SO) module to mitigate the impact caused by the uneven distribution of salient object areas. After that, considering that the inherent characteristics of multi-level features where high-level features have accurate location information, while low-level features have detailed spatial structure information, we propose the dense detail enhancement (DDE) module and mutual interaction semantic (MIS) module to extract and optimize the detail and location cues in the subsequent decoding stage. First, recognizing that object areas in natural scenes often have irregular appearances, we place the dense detail enhancement (DDE) modules in the features of the lower three layers, where the multiple dense connections are employed to facilitate the fusion of features with different receptive fields. Besides, we append four additional visual state space (VSS) blocks to further explore detailed information. Secondly, different from the DE module which leverages convolutional layers with higher dilated rates to extract structure cues, in the mutual interaction semantic (MIS) module, we just utilize convolutional layers with dilation rates of 1, 2, 3, and adopt the mutual fusion strategy to complete mutual interaction of information at different scales. Finally, cross-level connections are employed to integrate positional and spatial structural information, resulting in high-quality detection outcomes.

The main contributions of this paper are summarized as follows,

- 1) We propose a novel Region-guided Selective Optimization Network (RSONet) for RGB-T Salient Object Detection

which consists of the region guidance and saliency generation stages to resolve the issue of inconsistent salient information between the two modalities. Experimental results on public RGB-T dataset prove that our RSONet outperforms the other state-of-the-art saliency detection methods.

- 2) We propose the region guidance stage which includes three parallel branches and leverages the context interaction (CI) module and spatial fusion module to pick out the modality with the most accurate object information.
- 3) We propose the saliency generation stage to gain the high-quality final saliency map, where the selective optimization (SO) module is leveraged to integrate RGB and thermal features, the dense detail enhancement (DDE) module adopts convolutions with different dilation rates to dig the spatial structure information, and the mutual interaction semantic (MIS) module is placed in the high-level features to mine the location cues.

II. RELATED WORKS

In this section, we briefly review the salient object detection, including the single-modal SOD and multi-modal SOD.

A. Single-modal Salient Object Detection

In the last decade, many efforts have been spent in the one-modal [38] salient object detection. For example, In [39], Feng *et al.* introduced attentive feedback modules to effectively capture object structures. In [40], Zhang *et al.* proposed an end-to-end dense attention fluid network, utilizing a global context-aware attention module to capture long-range semantic relationships and a dense attention fluid structure to transfer shallow attention cues to deeper layers. In [41], Wang *et al.* developed a rectangular convolution pyramid and edge enhancement network, with the rectangular convolution pyramid module designed to characterize defects with diverse structures. In [42], Ma *et al.* proposed a bilateral extreme stripping encoder, a dynamic complementary attention module and a switch-path decoder to get the broader receptive fields and obtain the ability to perceive extreme large- or small-scale objects. In [43], Zhang *et al.* addressed challenges in utilizing edge cues and multi-level feature fusion persist by a two-stream model for saliency and edge detection, an edge-guided interaction module for feature enhancement, and specialized fusion modules for progressive integration of semantic and detailed information. In [44], Wang *et al.* proposed a fast and extremely lightweight end-to-end wavelet neural network which designs proposing a wavelet transform module, a wavelet transform fusion module and a novel feature residual mechanism for real-time salient object detection. In [45], presented the adaptive semantic network Including an adaptive semantic matching module for aligning global and local contexts, an adaptive feature enhancement module for enhancing salient regions and restoring resolution, and a multiscale fine-grained inference module for refining high-level semantics with low-level details to produce high-quality saliency maps.

B. Multi-modal Salient Object Detection

With advancements in image acquisition technology, depth modality has become widely utilized in salient object detection (SOD) tasks, offering complementary information to enhance detection accuracy. In [46], Huang *et al.* proposed a lightweight RGB-D SOD model that uses two shallow subnetworks to extract low- and middle-level features from unimodal RGB and depth inputs, ensuring efficient and accurate feature representation. Similarly, in [47], Song *et al.* introduced a modality-aware decoder designed to enhance multimodal integration through a series of feature embedding, modality reasoning, and feature back-projection and collection strategies, effectively improving the model's ability to handle complex scenes. In [48], Fang *et al.* proposed a novel group transformer network capable of capturing long-range dependencies across layer features, enhancing feature representation between high-level and low-level features. In [49], Feng *et al.* introduced a multimodal multilevel feature fusion module for enhanced RGB-D features, a multi-input aggregation module to integrate RGB and depth streams, and a saliency refinement module to eliminate redundancy and refine features before decoder integration. Depth information in RGB-D-based SOD methods is often influenced by the object's location, making it challenging to detect targets close to the background. To address this limitation, thermal images have been introduced as supplementary information for SOD. In [50], Chen *et al.* proposed a Cross-Guided Modality Difference Reduction Network that employs a modality difference reduction module, a cross-attention fusion module, and a transformer-based feature enhancement module to minimize modality differences. Similarly, in [51], He *et al.* introduced an Enhancement and Aggregation Feedback Network, incorporating a feature enhancement block and a cross-feature aggregation module to achieve effective multimodal complementation. In [52], Wang *et al.* proposed the intra-modality self-enhancement mirror network which presents the intra-modality cross-scale self-enhancement module to exploit saliency clues by modeling the correlation between intra-modality cross-scale features. In [53], Yue *et al.* proposed spatial-frequency feature exploration modules and spatial-frequency feature interaction modules to separate spatial-frequency feature and integrates cross-modality and cross-domain information for generating high-quality saliency maps. Furthermore, in [54], He *et al.* proposed a unified pure mamba-based framework, which redesigned the scanning strategy and upsampling process to preserve the spatial continuity of salient regions and enhance hierarchical feature aggregation for general SOD tasks. In [55], Liu *et al.* proposed a SAM-based SOD method, which addressed modality imbalance and gradient conflicts in RGB-T SOD by incorporating unimodal supervision, gradient deconfliction, and decoupled adapters to enhance foreground?background discrimination and improve model convergence and generalization.

III. PROPOSED FRAMEWORK

A. Overview of Proposed RSONet

In this paper, we propose a Region-guided Selective Optimization Network (RSONet) for RGB-T Saliency Object Detection, which comprises two stages: region guidance and saliency generation, to address the issue of inconsistent salient regions and yield high-quality saliency map. In the region guidance stage, three identical encoder-decoder structures are used to construct guidance maps \mathbf{G}^R , \mathbf{G}^T and \mathbf{G}^{RT} from the RGB image, the thermal image, and the sum of the RGB and thermal images, respectively, where the encoder adopts SwinTransformer [37] to extract multi-level features $\{\mathbf{F}_i^R\}_{i=1}^5$, $\{\mathbf{F}_i^T\}_{i=1}^5$ and $\{\mathbf{F}_i^{RT}\}_{i=1}^5$ from inputs, and the decoder first leverages convolutions of different kernel sizes in the context interaction (CI) module to extract contextual information $\{\mathbf{F}_i^{RC}\}_{i=1}^5$, $\{\mathbf{F}_i^{TC}\}_{i=1}^5$ and $\{\mathbf{F}_i^{RTC}\}_{i=1}^5$ from features at different levels. Then, the spatial-aware fusion (SF) module is designed to optimize context features, yielding the guidance maps. Next, \mathbf{G}^R and \mathbf{G}^T are each compared with \mathbf{G}^{RT} to calculate similarity, thereby selecting the modality with the most accurate object information. In the saliency generation stage, based on the previous similarity calculation results, the selective optimization (SO) module selectively optimizes and fuses the two modality features $\{\mathbf{F}_i^R\}_{i=1}^5$ and $\{\mathbf{F}_i^T\}_{i=1}^5$ extracted from the backbone network. Subsequently, considering the different characteristics of multi-level features, the dense detail enhancement (DDE) module and mutual interaction semantic (MIS) module are placed in low-level and high-level features, respectively, which employ different dilated convolution strategies to extract spatial structural information \mathbf{F}_i^D and positional information \mathbf{F}_i^M of the object. Finally, the cross-level connection is adopted to generate high-quality saliency map \mathbf{S}

B. Region Guidance Stage

Lighting and temperature variations often result in incomplete or unclear representations of the object region in both RGB and thermal images. Consequently, directly fusing the two modalities may introduce considerable noise from irrelevant regions, ultimately compromising detection performance. To mitigate this issue, we propose the region guidance stage, which consists of three identical encoder-decoder structures used to extract region guidance maps from the RGB image, the thermal image, and the sum of the RGB and thermal images, respectively, to select the modality with the most accurate object information and ensures it dominates the subsequent bimodal fusion stage.

1) *Context Interaction Module*: Taking the RGB branch as an example, to extract object contextual information from the multi-level features obtained by the backbone network (Swin Transformer). Considering that features at different levels exhibit distinct characteristics—high-level features have smaller spatial resolutions and capture object semantics and location, while low-level features retain larger spatial resolutions and preserve fine-grained structural details—uniformly optimizing or enhancing all levels of features during the decoding stage may obscure their unique contributions. For example, when

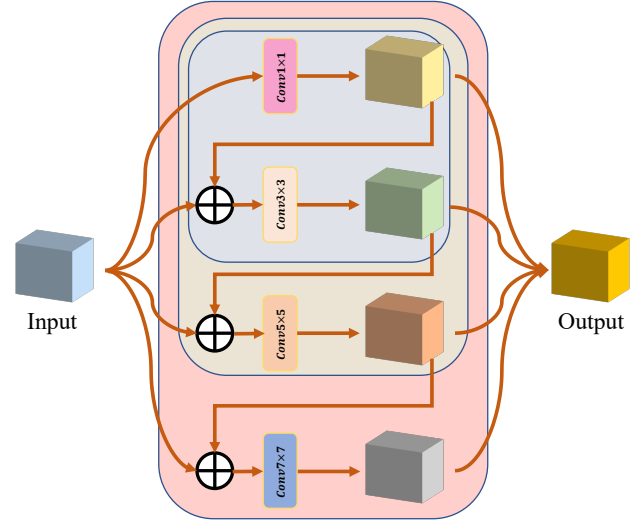


Fig. 4: Architecture of the context interaction module.

large convolutional kernels are applied to low-resolution features, they may integrate the target and surrounding background information indiscriminately. Conversely, when small kernels are applied to high-resolution features, the receptive field may be insufficient to capture the complete structure of the target object. To end this, we leverage convolutional layers with different kernel sizes and employ different contextual information extraction strategies for different levels of features. As shown in Fig. 4, the context interaction module consists of three variants (*i.e.*, pink, yellow and blue parts), which are applied to low-level feature \mathbf{F}_1^R , mid-level features $\mathbf{F}_{2/3}^R$, and high-level features $\mathbf{F}_{4/5}^R$, respectively. For the variant one (pink part), feature \mathbf{F}_1^R is fed into four parallel branches, each with different convolutional layers to extract contextual information at various scales. Besides, break down the barriers between features of different scales, we add the output of the previous branch to the input features of the current branch. Then, the results of the four branches are concatenated along the channel dimension to obtain the module's output \mathbf{F}_1^{RCI} ,

$$\begin{cases} \mathbf{F}_1^{R_1} = f_{1 \times 1}(\mathbf{F}_1^R) \\ \mathbf{F}_1^{R_2} = f_{3 \times 3}(\mathbf{F}_1^{R_1} + \mathbf{F}_1^R) \\ \mathbf{F}_1^{R_3} = f_{5 \times 5}(\mathbf{F}_1^{R_2} + \mathbf{F}_1^R) \\ \mathbf{F}_1^{R_4} = f_{7 \times 7}(\mathbf{F}_1^{R_3} + \mathbf{F}_1^R) \end{cases}, \quad (1)$$

where $f_{1 \times 1}$, $f_{3 \times 3}$, $f_{5 \times 5}$ and $f_{7 \times 7}$ mean the convolutional layers with kernel sizes of 1, 3, 5, and 7, respectively. For the mid-level features $\mathbf{F}_{2/3}^R$, considering their reduced resolution, using excessively large convolutional kernels would integrate a significant amount of irrelevant information. Therefore, compared to variant one, we remove the 7×7 convolutional branch,

$$\begin{cases} \mathbf{F}_{2/3}^{R_1} = f_{1 \times 1}(\mathbf{F}_{2/3}^R) \\ \mathbf{F}_{2/3}^{R_2} = f_{3 \times 3}(\mathbf{F}_{2/3}^{R_1} + \mathbf{F}_{2/3}^R) \\ \mathbf{F}_{2/3}^{R_3} = f_{5 \times 5}(\mathbf{F}_{2/3}^{R_2} + \mathbf{F}_{2/3}^R) \end{cases}. \quad (2)$$

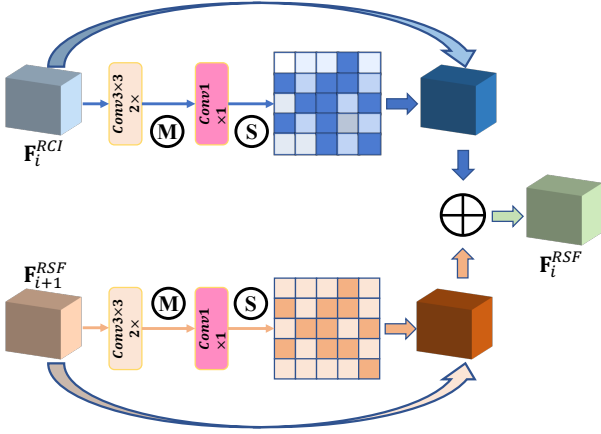


Fig. 5: Architecture of the spatial-aware fusion module.

Similarly, for the high-level features $\mathbf{F}_{4/5}^R$, building on the modifications in variant two, we further remove the 5×5 convolutional branch,

$$\begin{cases} \mathbf{F}_{4/5}^{R_1} = f_{1 \times 1}(\mathbf{F}_{4/5}^R) \\ \mathbf{F}_{4/5}^{R_2} = f_{3 \times 3}(\mathbf{F}_{4/5}^{R_1} + \mathbf{F}_{4/5}^R) \end{cases} \quad (3)$$

2) *Spatial-aware Fusion Module*: After the context interaction module, rich object information is digged out. However, the use of multiple convolutional layers of different sizes inevitably introduces irrelevant information, making it difficult to accurately reconstruct the object area. To address the issue, the spatial-aware fusion (SF) module is proposed to integrate features generated from the CI module, where the object cures are optimized in the spatial dimension. As shown in Fig. 5, first, two 3×3 convolutional layers are deployed to the context feature \mathbf{F}_i^{RCI} to further extract object information, obtaining feature \mathbf{F}_i^{RC} . Then, to achieve optimization in the spatial dimension, the global max pooling followed by 1×1 convolutional layer and sigmoid function is applied to generate the weighted feature \mathbf{W}_i^R which is multiplied and added with \mathbf{F}_i^{RC} to achieve feature optimization,

$$\begin{cases} \mathbf{F}_i^{RC} = f_{3 \times 3}(f_{3 \times 3}(\mathbf{F}_i^{RCI})) \\ \mathbf{W}_i^R = \sigma(f_{1 \times 1}(f_{Max}(\mathbf{F}_i^{RC}))) \\ \mathbf{F}_i^{RO} = \mathbf{F}_i^{RC} \times \mathbf{W}_i^R + \mathbf{F}_i^{RC} \end{cases} \quad (4)$$

For the feature \mathbf{F}_{i+1}^{RSF} yielded from the previous SF module, the same operations performed on feature \mathbf{F}_i^{RCI} are also carried out on feature \mathbf{F}_{i+1}^{RSF} . Finally, two optimized features are combined through addition to produce the output feature \mathbf{F}_i^{RSF} ,

$$\begin{cases} \mathbf{F}_{i+1}^{RC} = f_{3 \times 3}(f_{3 \times 3}(\mathbf{F}_{i+1}^{RSF})) \\ \mathbf{W}_{i+1}^R = \sigma(f_{1 \times 1}(f_{Max}(\mathbf{F}_{i+1}^{RC}))) \\ \mathbf{F}_{i+1}^{RO} = \mathbf{F}_{i+1}^{RC} \times \mathbf{W}_{i+1}^R + \mathbf{F}_{i+1}^{RC} \\ \mathbf{F}_i^{RSF} = \mathbf{F}_i^{RO} + \mathbf{F}_{i+1}^{RO} \end{cases} \quad (5)$$

where f_{Max} means the global max pooling and σ denotes the sigmoid function.

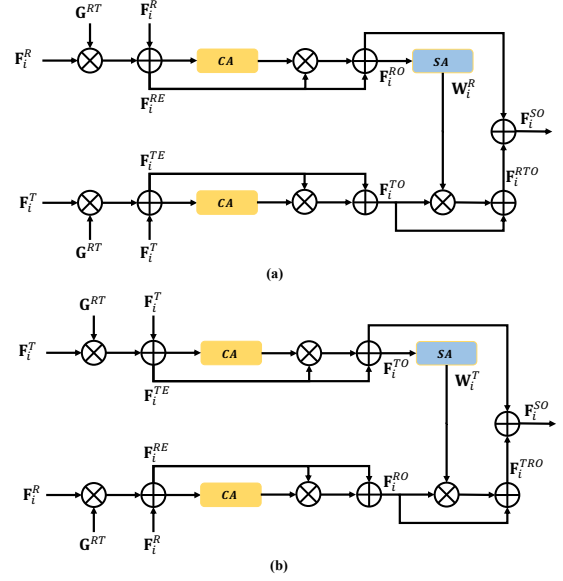


Fig. 6: Architecture of the selective optimization module.

3) *Similarity calculation*: To select the modality containing accurate object information, we first leverage 1×1 convolutional layer and sigmoid function to generate three guidance maps \mathbf{G}^R , \mathbf{G}^T and \mathbf{G}^{RT} ,

$$\begin{cases} \mathbf{G}^R = \sigma(f_{1 \times 1}(\mathbf{F}_1^{RSF})) \\ \mathbf{G}^T = \sigma(f_{1 \times 1}(\mathbf{F}_1^{TSF})) \\ \mathbf{G}^{RT} = \sigma(f_{1 \times 1}(\mathbf{F}_1^{RTSF})) \end{cases} \quad (6)$$

Then, we compute the sum of all elements in each of the three guidance maps, obtaining three values M^R , M^T and M^{RT} . After that, M^R and M^T are each compared with M^{RT} , and the smaller the difference, the more accurate the object information in the corresponding modality,

$$\begin{cases} M^R = \frac{1}{W \times H} \sum_{x=1}^W \sum_{y=1}^H \mathbf{G}^R(x, y) \\ M^T = \frac{1}{W \times H} \sum_{x=1}^W \sum_{y=1}^H \mathbf{G}^T(x, y) \\ M^{RT} = \frac{1}{W \times H} \sum_{x=1}^W \sum_{y=1}^H \mathbf{G}^{RT}(x, y) \end{cases} \quad (7)$$

C. Saliency Generation Stage

Following the region guidance stage, which selects the modality with more reliable object information, we design a series of modules—namely, the selective optimization (SO) module, dense detail enhancement (DDE) module, and mutual interaction semantic (MIS) module—to effectively exploit and integrate complementary bimodal features, thereby facilitating accurate and robust saliency prediction.

1) *Selective Optimization Module*: As shown in Fig. 6 (a), where the RGB image contains richer object information compared to the thermal image. First, RGB feature \mathbf{F}_i^R and thermal feature \mathbf{F}_i^T are each multiplied and added with guidance map \mathbf{G}^{RT} to perform an initial optimization and enhancement of the two modality features, yielding \mathbf{F}_i^{RE} and \mathbf{F}_i^{TE} . Then, although the introduction of guidance map \mathbf{G}^{RT} enhances the bimodal features to some extent, it inevitably introduces some interference since it is not an accurate saliency map. Therefore,

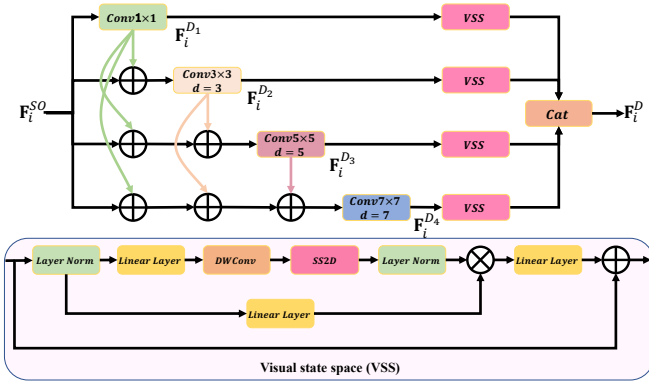


Fig. 7: Architecture of the dense detail enhancement module.

we apply the channel attention operation which consists of 1×1 convolutional layer, global average pooling and sigmoid function to feature \mathbf{F}_i^{RE} and feature \mathbf{F}_i^{TE} for gaining vectors \mathbf{V}_i^R and \mathbf{V}_i^T . After that, two feature vectors are each multiplied and added to their corresponding features to complete the channel dimension feature optimization, obtaining features \mathbf{F}_i^{RO} and \mathbf{F}_i^{TO} ,

$$\begin{cases} \mathbf{F}_i^{RE} = \mathbf{F}_i^R \times \mathbf{G}^{RT} + \mathbf{F}_i^R \\ \mathbf{F}_i^{TE} = \mathbf{F}_i^T \times \mathbf{G}^{RT} + \mathbf{F}_i^T \\ \mathbf{F}_i^{RO} = f_{CA}(\mathbf{F}_i^{RE}) \times \mathbf{F}_i^{RE} + \mathbf{F}_i^{RE} \\ \mathbf{F}_i^{TO} = f_{CA}(\mathbf{F}_i^{TE}) \times \mathbf{F}_i^{TE} + \mathbf{F}_i^{TE} \end{cases} \quad (8)$$

Considering that the RGB image contains richer object information than the thermal image in the current context, we apply spatial attention operations to feature \mathbf{F}_i^{RO} . The resulting weighted feature \mathbf{W}_i^R is then multiplied and added with feature \mathbf{F}_i^{TO} to achieve the optimization of the thermal image by the RGB image and generate \mathbf{F}_i^{RTO} . Finally, the optimized features \mathbf{F}_i^{RO} and \mathbf{F}_i^{RTO} are combined through addition to produce the output \mathbf{F}_i^{SO} ,

$$\begin{cases} \mathbf{F}_i^{RTO} = f_{SA}(\mathbf{F}_i^{RO}) \times \mathbf{F}_i^{TO} + \mathbf{F}_i^{TO} \\ \mathbf{F}_i^{SO} = \mathbf{F}_i^{RO} + \mathbf{F}_i^{RTO} \end{cases} \quad (9)$$

where f_{CA} and f_{SA} denote the channel attention and spatial attention, respectively. Additionally, in another scenario where the thermal image contains more object information than the RGB image, the two modality features are fused according to the method shown in Fig. 6 (b) to produce the feature \mathbf{F}_i^{SO} .

2) *Dense Detail Enhancement Module*: Considering that low-level features at high-resolution scales contain rich spatial structure information, inspired by the Atrous Spatial Pyramid Pooling (ASPP), we develop the dense detail enhancement (DDE) module. As shown in Fig. 7, the DDE module employs four parallel branches, each utilizing convolutional layers with different sizes and dilation rates to capture target information at various receptive fields. Additionally, in the ASPP, the output features from branches with different receptive fields are often fused through concatenation, which overlooks the relationships between these features. To address this, we incorporate dense connections within the DDE module, adding

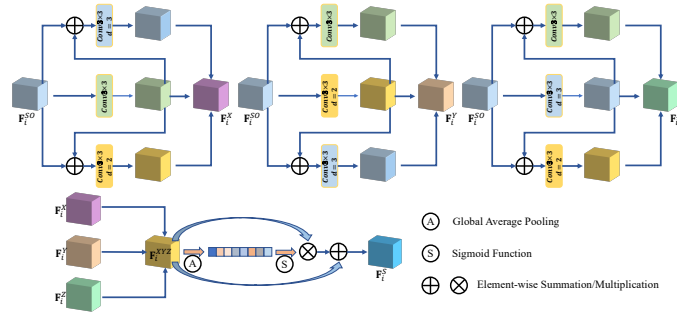


Fig. 8: Architecture of the mutual interaction semantic module.

the receptive field features of the current branch to the input feature of the subsequent branches,

$$\begin{cases} \mathbf{F}_i^{D1} = f_{1 \times 1}(\mathbf{F}_i^{SO}) \\ \mathbf{F}_i^{D2} = f_{3 \times 3, 3}(\mathbf{F}_i^{D1} + \mathbf{F}_i^{SO}) \\ \mathbf{F}_i^{D3} = f_{5 \times 5, 5}(\mathbf{F}_i^{D1} + \mathbf{F}_i^{D2} + \mathbf{F}_i^{SO}) \\ \mathbf{F}_i^{D4} = f_{7 \times 7, 7}(\mathbf{F}_i^{D1} + \mathbf{F}_i^{D2} + \mathbf{F}_i^{D3} + \mathbf{F}_i^{SO}) \end{cases} \quad (10)$$

Besides, to further capture the spatial relationship of object, we place a visual state space (VSS) block on each branch, and the output features of these blocks are concatenated along the channel dimension to obtain the output features of the DDE module,

$$\mathbf{F}_i^D = \text{Cat}(VSS(\mathbf{F}_i^{D1}), VSS(\mathbf{F}_i^{D2}), VSS(\mathbf{F}_i^{D3}), VSS(\mathbf{F}_i^{D4})). \quad (11)$$

3) *Mutual Interaction Semantic Module*: In natural scenes, the positions of objects are often random, making traditional methods that use attention mechanisms ineffective in accurately locating object areas, thereby reducing detection accuracy. Therefore, for high-level features, we design the mutual interaction semantic (MIS) module to further optimize location information. As shown in Fig. 8, the MIS module employs a dense connection strategy similar to the DDE Module. However, considering the smaller resolution of high-level features, the MIS module only utilizes 3×3 convolutions with dilation rates of 1, 2, and 3. Specifically, the MIS module consists of three main branches with different fusion methods, each containing three sub-branches. Each sub-branch employs 3×3 convolutions with different dilation rates. To enable interaction among different receptive fields, the output of each sub-branch is added to the input features of the other two sub-branches. Then, the features of three sub-branches are fused through concatenation to obtain features \mathbf{F}_i^X , \mathbf{F}_i^Y and \mathbf{F}_i^Z .

$$\begin{cases} \mathbf{F}_i^{X1} = f_{3 \times 3}(\mathbf{F}_i^{SO}) \\ \mathbf{F}_i^{X2} = f_{3 \times 3, 2}(\mathbf{F}_i^{X1} + \mathbf{F}_i^{SO}) \\ \mathbf{F}_i^{X3} = f_{3 \times 3, 3}(\mathbf{F}_i^{X1} + \mathbf{F}_i^{SO}) \\ \mathbf{F}_i^X = f_{3 \times 3}(\text{Cat}(\mathbf{F}_i^{X1}, \mathbf{F}_i^{X2}, \mathbf{F}_i^{X3})) \end{cases} \quad (12)$$

$$\begin{cases} \mathbf{F}_i^{Y1} = f_{3 \times 3, 2}(\mathbf{F}_i^{SO}) \\ \mathbf{F}_i^{Y2} = f_{3 \times 3}(\mathbf{F}_i^{Y1} + \mathbf{F}_i^{SO}) \\ \mathbf{F}_i^{Y3} = f_{3 \times 3, 3}(\mathbf{F}_i^{Y1} + \mathbf{F}_i^{SO}) \\ \mathbf{F}_i^Y = f_{3 \times 3}(\text{Cat}(\mathbf{F}_i^{Y1}, \mathbf{F}_i^{Y2}, \mathbf{F}_i^{Y3})) \end{cases} \quad (13)$$

$$\begin{cases} \mathbf{F}_i^{Z_1} = f_{3 \times 3, 3}(\mathbf{F}_i^{SO}) \\ \mathbf{F}_i^{Z_2} = f_{3 \times 3}(\mathbf{F}_i^{Z_1} + \mathbf{F}_i^{SO}) \\ \mathbf{F}_i^{Z_3} = f_{3 \times 3, 2}(\mathbf{F}_i^{Z_1} + \mathbf{F}_i^{SO}) \\ \mathbf{F}_i^Z = f_{3 \times 3}(\text{Cat}(\mathbf{F}_i^{Z_1}, \mathbf{F}_i^{Z_2}, \mathbf{F}_i^{Z_3})) \end{cases} \quad (14)$$

Similarly, the output features of the three main branches are concatenated and fused, with a channel attention mechanism applied to suppress irrelevant information to some extent, yielding the semantic feature \mathbf{F}_i^S ,

$$\begin{cases} \mathbf{F}_i^{XYZ} = f_{3 \times 3}(\text{Cat}(\mathbf{F}_i^X, \mathbf{F}_i^Y, \mathbf{F}_i^Z)) \\ \mathbf{F}_i^S = f_{CA}(\mathbf{F}_i^{XYZ}) \times \mathbf{F}_i^{XYZ} + \mathbf{F}_i^{XYZ} \end{cases}, \quad (15)$$

where $f_{3 \times 3}$, $f_{3 \times 3, 2}$ and $f_{3 \times 3, 3}$ mean the convolutional layers with dilated rates of 1, 2, and 3, respectively.

D. Deep Supervision

To promote the performance of RSONet, we adopt the fusion loss, which consists of binary cross entropy (BCE) loss [56], boundary intersection over union (IOU) loss [57] and F-measure (FM) loss [58] to supervise five saliency maps. The loss function L_{total} is formulated as follows,

$$L_{total} = \frac{1}{N} \sum_{i=1}^N (L_{bce} + L_{iou} + L_{fm}), \quad (16)$$

where N is batch size of training phase.

IV. EXPERIMENTS AND ANALYSES

A. Implementation Details and Evaluation Metrics

1) *Implementation Details:* We train and test our RSONet on three public RGB-T datasets, including VT5000 [65], VT1000 [81], and VT821 [82]. The VT5000 is a large-scale RGB-T dataset and contains 5000 images of all day scenes, of which 2500 images are the training dataset and the other 2500 images are the test dataset. VT1000 and VT821 includes 1000 and 821 registered RGB-T images, which are taken as the test set. Our proposed network is conducted based on the Pytorch toolbox, and we implement it on a computing station with a single NVIDIA GeForce RTX 4080 GPU. In this article, for the backbone network of our RSONet, we utilize the SwinTransformer model [37], which has been pre-trained on the ImageNet dataset [83]. Other network parameters are initialized randomly. Before the training process, training and test images are resized to 384×384 for minimizing the utilization of computing resources. Besides, to optimize the training process, we select the RMSprop optimizer [84] to minimize the loss function, where the learning rate and momentum are set $1e-4$ and 0.9 , respectively.

2) *Evaluation Metrics:* To evaluate the performance of our proposed RSONet, we choose five evaluation metrics, including mean absolute error (M) [85], F-measure (F_β) [86], E-measure (E_ξ) [87], Structure-measure (S_α) [88]. The mathematical definitions of all metrics are depicted as follows,

B. Comparison with State-of-the-Art Methods

In experiments, we compare the proposed RSONet with other 27 state-of-the-art salient object detection methods, including ADF [65], MIDD [59], SPNet [73], UidefNet [69], HRTransNet [68], WaveNet [72], SwinNet [37], CAVER [71], CCFFNet [67], MCFNet [34], TNet [66], CGFNet [64], APNet [63], TAGFNet [70], ECFFNet [62], CSRNet [61], MMIR [74], SMRNet [80], ISMNet [52], DSCDNet [79], DFENet [77], LAFB [76], PATNet [75], MMNet [60], ContriNet [78], Samba [54] and SAMSOD [55]. To ensure a fair comparison, we used the source code released online by the authors.

1) *Qualitative Comparison:* To demonstrate the effectiveness of our RSONet, we list some visualization results of challenging scenes from RGB and thermal images, as shown in Fig. 9, where the object region and background exhibit similar thermal radiation in thermal maps (rows 1-4), the object appears under low-light conditions in RGB images (rows 5-6), and the object demonstrates complex appearance contours in the images (rows 6-12).

For the challenges of similar thermal radiation, we can observe that the object region often shares similar thermal radiation characteristics with the background in the thermal images, significantly increasing the complexity and challenges of detection. Consequently, most SOD methods relying solely on RGB images frequently fail to achieve accurate segmentation of the salient object. Specifically, as illustrated in Fig. 9 (the 1st row), the chair is clearly visible in the RGB image; however, in the thermal map, the chair's thermal radiation closely resembles that of the background. From it, we observe that nearly all comparison methods fail to fully reconstruct the various parts of the chair, with methods CAVER [71] and WaveNet [72] are able to identify only the seat surface, and methods TAGFNet [70], APNet [63], CGFNet [64] and TNet [66] mistakenly identify the door frame area as a significant object. For the challenges of low-light condition, as shown in Fig. 9 (rows 5-6), we can see that objects are barely distinguishable in RGB images, which significantly hinders detection. For instance, in the RGB image of the 6th row, where only the side of the box is visible, most detection methods (*i.e.*, MMNet [60], CSRNet [61], and HRTransNet [68]) only highlight a partial area of the object. Furthermore, detection results from other methods also exhibit missing regions in certain areas. For the other images (rows 6-12) which contain the challenges of complex appearance contours, it can be observed that various comparison methods (*i.e.*, MIDD [59], ECFFNet [62]) exhibit a certain degree of false positives or omissions. Analysis of the above visualization results reveals that our method RSONet demonstrates greater robustness and achieves superior performance across all challenging scenes.

2) *Quantitative comparison:* In this part, we list the quantitative performance comparisons of our RSONet with other twenty-nine SOD methods in terms of four evaluation metrics (*i.e.*, M , F_β , S_α , E_ξ), as shown in in Table. I, where the numerical results reveal that our proposed method performs better than others on RGB-T datasets (*i.e.*, VT821, VT1000, and VT5000). To be specific, compare to state of the art method PATNet [75], our RSONet achieves optimal results

TABLE I: Quantitative comparisons with 27 methods on three RGB-T datasets. The top three results in each column are marked with red, blue, green color, respectively. \uparrow and \downarrow denote that larger value is better and smaller value is better, respectively.

Methods		VT5000				VT1000				VT821				
		$\mathcal{M} \downarrow$	$F_\beta \uparrow$	$S_\alpha \uparrow$	$E_\xi \uparrow$	$\mathcal{M} \downarrow$	$F_\beta \uparrow$	$S_\alpha \uparrow$	$E_\xi \uparrow$	$\mathcal{M} \downarrow$	$F_\beta \uparrow$	$S_\alpha \uparrow$	$E_\xi \uparrow$	
RGB-T	MIDD [59]	TIP ₂₁	.046	.788	.856	.893	.029	.870	.907	.935	.045	.803	.871	.897
	MMNet [60]	TCSVT ₂₁	.044	.777	.863	.888	.027	.859	.914	.931	.040	.792	.874	.893
	CSRNet [61]	TCSVT ₂₁	.042	.809	.868	.907	.024	.875	.918	.939	.038	.829	.885	.912
	ECFFNet [62]	TCSVT ₂₁	.038	.803	.875	.911	.022	.873	.924	.947	.035	.807	.877	.907
	APNet [63]	TETC ₁₂₁	.035	.816	.876	.917	.022	.880	.922	.950	.034	.814	.868	.911
	CGFNet [64]	TCSVT ₂₁	.035	.851	.883	.924	.024	.901	.921	.953	.036	.842	.879	.915
	ADF [65]	TMM ₂₂	.048	.778	.864	.891	.034	.846	.909	.922	.077	.716	.810	.844
	TNet [66]	TMM ₂₂	.033	.845	.895	.929	.021	.887	.929	.952	.030	.840	.899	.924
	CCFENet [67]	TCSVT ₂₂	.031	.858	.896	.937	.018	.904	.934	.962	.027	.856	.900	.933
	SwinNet [37]	TCSVT ₂₁	.026	.864	.912	.945	.018	.894	.938	.957	.030	.846	.904	.928
	HRTransNet [68]	TCSVT ₂₂	.025	.869	.913	.948	.017	.898	.938	.956	.026	.851	.906	.933
	UidefNet [69]	EAAI ₂₂	.025	.874	.914	.948	.015	.911	.941	.969	.023	.872	.917	.945
	MCFNet [34]	AI ₂₃	.033	.846	.888	.928	.019	.900	.932	.960	.029	.842	.891	.925
	TAGFNet [70]	EAAI ₂₃	.036	.826	.884	.916	.021	.888	.926	.951	.035	.821	.881	.909
	CAVER [71]	TIP ₂₃	.029	.854	.900	.940	.017	.904	.938	.965	.027	.853	.898	.934
	WaveNet [72]	TIP ₂₃	.026	.863	.912	.944	.015	.905	.945	.967	.025	.854	.912	.935
	SPNet [73]	ACM MM ₂₃	.024	.885	.915	.952	.015	.918	.942	.972	.023	.874	.914	.943
	MMIR [74]	TIM ₂₄	.031	.879	.889	.936	.019	.927	.938	.955	.030	.866	.885	.923
	PATNet [75]	KBS ₂₄	.023	.880	.916	.951	.015	.908	.941	.964	.024	.868	.914	.938
	LAFB [76]	TCSVT ₂₄	.030	.856	.893	.934	.018	.903	.932	.960	.034	.841	.884	.922
	DFENet [77]	arXiv ₂₄	.023	.882	.920	.950	.015	.901	.948	.958	.023	.871	.917	.938
	ContriNet [78]	TPAMI ₂₅	.022	.878	.915	.940	.015	.918	.941	.954	.020	.898	.923	.956
	Samba [54]	CVPR ₂₅	.021	.894	.926	.958	.013	.926	.952	.976	.018	.894	.934	.955
	SAMSOD [55]	TMM ₂₆	.021	.921	.923	.964	.015	.942	.942	.976	.022	.895	.913	.950
	DSCDNet [79]	TCE ₂₅	.023	.888	.918	.949	.014	.921	.946	.955	.022	.876	.904	.915
	SMRNet [80]	AAAI ₂₅	.030	.859	.891	.935	.020	.899	.924	.945	.030	.844	.888	.920
	ISMNet [52]	TCSVT ₂₅	.025	.885	.913	.945	.014	.922	.942	.954	.021	.886	.917	.945
Ours		.020	.910	.926	.963	.014	.923	.946	.972	.021	.883	.921	.946	

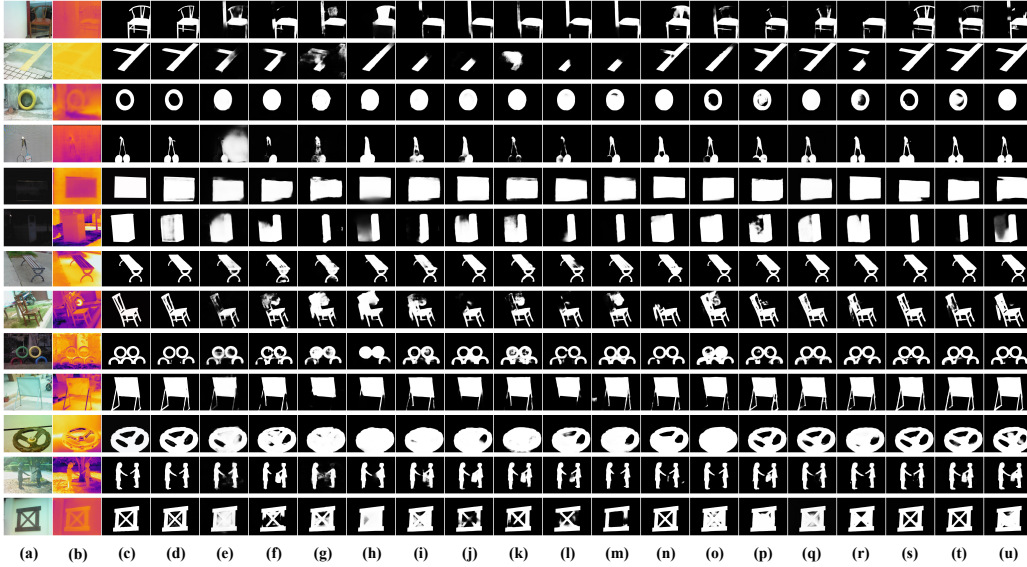


Fig. 9: Visual comparisons with some methods on RGB-T datasets. The predictions of compared method are listed in each column. (a) RGB images, (b) thermal images, (c) ground truth, (d) Ours, (e) ADF [65], (f) MIDD [59], (g) MMNet [60], (h) CSRNet [61], (i) ECFFNet [62], (j) TAGFNet [70], (k) APNet [63], (l) CGFNet [64], (m) TNet [66], (n) MCFNet [34], (o) CCFENet [67], (p) CAVER [71], (q) SwinNet [37], (r) WaveNet [72], (s) HRTransNet [68], (t) UidefNet [69], (u) SPNet [73]

TABLE II: Comparison of the model parameter, complexity and the average running speed.

Method	MIDD	CGFNet	TNet	SwinNet	TAGFNet	LAFB	PATNet	Samba
Speed(FPS)	42.2	52.3	49.6	30.9	39.5	43	10.6	-
Params(M)	52.4	69.9	87	198.8	36.2	453	94.9	54.9
FLOPs(G)	216.7	347.8	39.7	124.7	115.1	139.7	51.1	71.6
Method	WaveNet	DFENet	DSCDNet	SMRNet	ISMNet	SAMSOD	ContriNet	Ours
Speed(FPS)	7.7	11.7	9.6	32.5	6.1	9.4	-	9.4
Params(M)	30.2	149.6	92.3	31.5	114.3	32.7	96.3	88
FLOPs(G)	26.7	139.5	134.1	45.3	100.4	418.0	126.9	143.8

1.2% and 1.1% on VT5000, and F_β and E_ξ increase by 1.7% and 0.8% on VT1000. Furthermore, Table. II presents the model parameters, icomplexity and detection speeds of several representative methods. As shown, the proposed model benefits from the parameter-sharing strategy, which effectively controls the number of parameters and keeps it at a moderate level compared with existing approaches. Nevertheless, due to the adoption of a two-stage design, the detection speed is relatively lower, reflecting the trade-off between structural refinement and computational efficiency.

on VT5000 and delivers competitive performance on VT1000 and VT5000, where F_β , E_ξ and S_α increase by 3.4% ,

TABLE III: Ablation study on different component.

Settings	$M\downarrow$	$F_\beta\uparrow$	$S_\alpha\uparrow$	$E_\xi\uparrow$
w/o SO (Addition)	0.0217	0.8883	0.9213	0.9523
w/o SO (Multiplication)	0.0208	0.8948	0.9231	0.9587
w/o SO (Concatenation)	0.0215	0.8896	0.9224	0.9558
w/o SO (Pixel-wise)	0.0203	0.8951	0.9239	0.9605
R \rightarrow T	0.0215	0.8898	0.9230	0.9561
T \rightarrow R	0.0216	0.8896	0.9233	0.9554
w/o DDE	0.0203	0.9082	0.9213	0.9631
w/o MIS	0.0203	0.8997	0.9241	0.9593
w/o DDE & MIS	0.0217	0.9053	0.8995	0.9556
Ours	0.0197	0.9071	0.9261	0.9632

TABLE IV: Ablation study on different backbone.

Settings	$M\downarrow$	$F_\beta\uparrow$	$S_\alpha\uparrow$	$E_\xi\uparrow$
ResNet-18	0.0408	0.8012	0.8618	0.9052
ResNet-34	0.0358	0.8146	0.8770	0.9125
ResNet-50	0.0413	0.7965	0.8638	0.8994
SAM	0.0438	0.8222	0.8409	0.9074
DINO	0.0372	0.8562	0.8751	0.9258
Ours	0.0197	0.9071	0.9261	0.9632

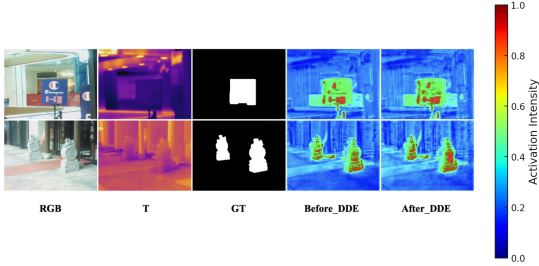


Fig. 10: Illustration of the impact of dense detail enhancement module.

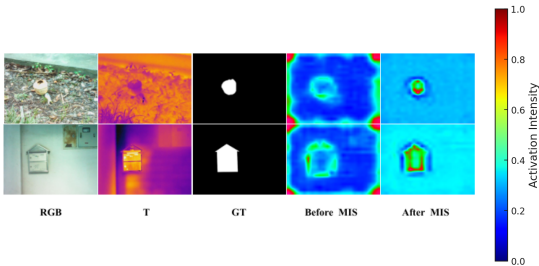


Fig. 11: Illustration of the impact of mutual interaction semantic module.

C. Ablation Study

To show the effectiveness of each component in our RSONet (*i.e.*, SO, DDE and MIS), and the different role of loss function and backbone, we conduct several ablation experiments, all numerical results are presented in Table. III and Table. IV.

To validate the functionality of each module, we conduct multiple experiments, all numerical results are listed in Table. III. First, to demonstrate the effectiveness of the selective optimization module, we remove the region guidance stage and replace the SO module with addition, multiplication, or concatenation to integrate the RGB and thermal features, respectively. From the comparison results in Table. III (rows

1-3 and 10), we can see that with the absence of SO module, low-quality features are directly fused with high-quality features, leading to varying degrees of detection performance degradation. In addition, in the fourth row of the Table. III, we replace the selective optimization module with a Pixel-wise Soft Gating strategy, in which a sigmoid map is used to weight the RGB and thermal features at each pixel. As shown by the results, although this strategy outperforms simple addition, multiplication, or concatenation, it still leads to a noticeable performance degradation. Then, we design two experiments (*i.e.*, R \rightarrow T and T \rightarrow R), where the whole region guidance stage is deleted and the two modalities features are directly fused according to Fig. 6 (a) or Fig. 6 (b). Due to the cancellation of the region guidance stage, the dual-modal feature fusion method without similarity calculation will result in low-quality feature maps being used to optimize high-quality feature maps, thereby reducing detection accuracy, which is further confirmed by the results in Table III (rows 5-6 and 10). After that, we successively conduct three experiments (*i.e.*, *w/o* DDE, *w/o* MIS and *w/o* DDE & MIS). To be specific, for the *w/o* DDE, we remove the dense detail enhancement (DDE) module and merge the high-level features from the mutual interaction semantic (MIS) module with the low-level features from the selective optimization (SO) module in a bottom-up manner to generate the final saliency map. Besides, for the *w/o* MIS, we remove the MIS module and similarly integrate high-level features from the SO module with the low-level features from the DDE module in a bottom-up manner. Furthermore, we remove both DDE module and MIS module in the *w/o* DDE & MIS, and directly fuse the multi-level features generated from the SO module. From Table. III (rows 7-10), we observe a decline in network performance with the removal of key module. Moreover, we visualize the feature maps before and after the application of DDE module and MIS module, as shown in Fig. 10 and Fig. 11. For instance, the feature map generated before the SO module primarily focuses on the approximate location of the salient object, whereas the feature map produced after the SO module accurately highlights the precise location of the object. To further evaluate the impact of different backbone, we replace the SwinTransformer [37] with ResNet-18 [89], ResNet-34 [89] and ResNet-50 [89] as shown in Table. IV. Compared to ResNet-18, our model gains improvement of 13.2% in terms of F_β and 7.4% in terms of S_α , respectively. In addition, compared to ResNet-34 and ResNet-50, our method demonstrates varying degrees of performance improvement, indicating that SwinTransformer possesses stronger feature extraction capabilities than ResNet-18, ResNet-34 and ResNet-50. Moreover, we attempt to replace the SwinTransformer adopted in this paper with stranger feature extractors (*i.e.*, SAM and DINO). As shown by the results in Table. IV, the model performance does not improve with the use of these large models; instead, it even degrades. This phenomenon can be attributed to the fact that frozen large-scale models are not well adapted to RGB-T imagery, and thus require dedicated adaptor to effectively exploit their representations in this task.

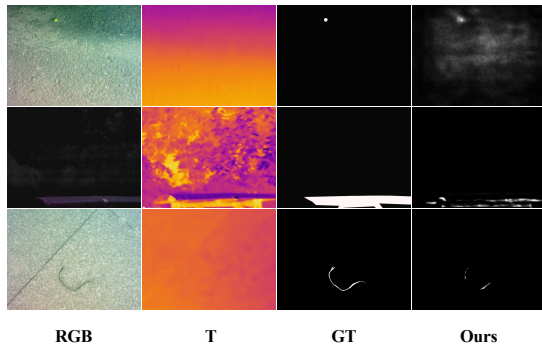


Fig. 12: Example of failure case.

D. Failure Cases

To give a comprehensive presentation of our RSONet, we list some failure cases. As shown in Fig. 12 (the 1st and 3th rows), when the salient objects in an image are extremely small or fine, our network struggles to detect them accurately. Besides, when both RGB images and thermal maps are in low quality, as shown in Fig. 12 (the 2nd row), even with the use of region guidance stage and the selective optimization module, the selected feature maps still contain significant noise, severely impacting the detection results.

V. CONCLUSION

This paper proposes a novel RGB-T salient object detection network called RSONet, which includes a region guidance stage and saliency generation stage. The region guidance stage employs the encoder-decoder structure which consists of the context interaction (CI) module and spatial-aware fusion (SF) module to yield the guidance maps from RGB, thermal, and RGBT images. Then, the saliency generation stage determines the dominant modal feature for fusion within the selective optimization (SO) module by calculating the similarity of the guidance maps. Besides, the dense detail enhancement (DDE) module and mutual interaction semantic (MIS) module are proposed to optimize the detail and location information. Overall, the proposed RSONet shows competitive results in RGB-T salient object detection compared with other twenty-eight state-of-the-art methods. In future work, we plan to explore more effective strategies for capturing and leveraging the complementary information between RGB and thermal modalities, further extending the applicability and robustness of our approach.

REFERENCES

- [1] G. Ma, S. Li, C. Chen, A. Hao, and H. Qin, "Rethinking image salient object detection: Object-level semantic saliency reranking first, pixelwise saliency refinement later," *IEEE Transactions on Image Processing*, vol. 30, pp. 4238–4252, 2021.
- [2] D. Jing, S. Zhang, R. Cong, and Y. Lin, "Occlusion-aware bi-directional guided network for light field salient object detection," in *Proceedings of the 29th ACM international conference on multimedia*, 2021, pp. 1692–1701.
- [3] G. Li, Z. Liu, D. Zeng, W. Lin, and H. Ling, "Adjacent context coordination network for salient object detection in optical remote sensing images," *IEEE Transactions on Cybernetics*, vol. 53, no. 1, pp. 526–538, 2022.
- [4] X. Zhou, K. Shen, and Z. Liu, "Admnet: Attention-guided densely multi-scale network for lightweight salient object detection," *IEEE Transactions on Multimedia*, 2024.
- [5] R. Cong, Z. Chen, H. Fang, S. Kwong, and W. Zhang, "Breaking barriers, localizing saliency: A large-scale benchmark and baseline for condition-constrained salient object detection," *IEEE Transactions on Pattern Analysis and Machine Intelligence*, 2025.
- [6] B. Wan, R. Cong, X. Zhou, H. Fang, Y. Sun, and S. Kwong, "Rdnet: Region proportion-aware dynamic adaptive salient object detection network in optical remote sensing images," *IEEE Transactions on Geoscience and Remote Sensing*, 2025.
- [7] Q. Qin, R. Cong, G. Zhan, Y. Liao, and S. Kwong, "From sight to insight: Unleashing eye-tracking in weakly supervised video salient object detection," *IEEE Transactions on Multimedia*, 2025.
- [8] B. Wan, R. Cong, X. Zhou, H. Fang, C. Lv, and S. Kwong, "G 2 hfnet: Geogran-aware hierarchical feature fusion network for salient object detection in optical remote sensing images," *IEEE Transactions on Circuits and Systems for Video Technology*, 2026.
- [9] T. Zhou, L. Li, X. Li, C.-M. Feng, J. Li, and L. Shao, "Group-wise learning for weakly supervised semantic segmentation," *IEEE Transactions on Image Processing*, vol. 31, pp. 799–811, 2021.
- [10] R. Cong, H. Yang, Q. Jiang, W. Gao, H. Li, C. Wang, Y. Zhao, and S. Kwong, "Bcs-net: Boundary, context, and semantic for automatic covid-19 lung infection segmentation from ct images," *IEEE Transactions on Instrumentation and Measurement*, vol. 71, pp. 1–11, 2022.
- [11] R. Cong, H. Xiong, J. Chen, W. Zhang, Q. Huang, and Y. Zhao, "Query-guided prototype evolution network for few-shot segmentation," *IEEE Transactions on Multimedia*, vol. 26, pp. 6501–6512, 2024.
- [12] X. Peng, J. Cheng, X. Tang, Z. Deng, W. Tu, and N. Xiong, "Hsnet: an intelligent hierarchical semantic-aware network system for real-time semantic segmentation," *IEEE Transactions on Systems, Man, and Cybernetics: Systems*, 2024.
- [13] R. Cong, A. Wang, B. Wan, C. Zhang, X. Zhou, and W. Zhang, "Divide-and-conquer decoupled network for cross-domain few-shot segmentation," *arXiv preprint arXiv:2511.07798*, 2025.
- [14] Z. Chen, C. Zhang, H. Fang, and R. Cong, "Empowering dino representations for underwater instance segmentation via aligner and prompter," *arXiv preprint arXiv:2511.08334*, 2025.
- [15] H. Xiong, R. Cong, J. Chen, C. Zhang, F. Li, H. Bai, and S. Kwong, "Mm-prompt: Multi-modality and multi-granularity prompts for few-shot segmentation," in *Proceedings of the 33rd ACM International Conference on Multimedia*, 2025, pp. 3067–3075.
- [16] R. Cong, Z. Yu, H. Fang, H. Sun, and S. Kwong, "Uis-mamba: exploring mamba for underwater instance segmentation via dynamic tree scan and hidden state weaken," in *Proceedings of the 33rd ACM International Conference on Multimedia*, 2025, pp. 343–352.
- [17] J. Chen, R. Cong, Y. Luo, H. H. S. Ip, and S. Kwong, "Replay without saving: Prototype derivation and distribution rebalance for class-incremental semantic segmentation," *IEEE transactions on pattern analysis and machine intelligence*, 2025.
- [18] R. Chen, B. Zheng, H. Zhang, Q. Chen, C. Yan, G. Slabaugh, and S. Yuan, "Improving dynamic hdr imaging with fusion transformer," in *Proceedings of the AAAI Conference on Artificial Intelligence*, vol. 37, no. 1, 2023, pp. 340–349.
- [19] B. Zheng, H. Li, Q. Chen, T. Wang, X. Zhou, Z. Hu, and C. Yan, "Quad bayer joint demosaicing and denoising based on dual encoder network with joint residual learning," in *Proceedings of the AAAI Conference on Artificial Intelligence*, vol. 38, no. 7, 2024, pp. 7552–7561.
- [20] K. Jiang, Q. Wang, Z. An, Z. Wang, C. Zhang, and C.-W. Lin, "Mutual retinex: Combining transformer and cnn for image enhancement," *IEEE Transactions on Emerging Topics in Computational Intelligence*, 2024.
- [21] Z. Liu, B. Zheng, Q. Chen, Q. Zhang, X. Jia, J. Zhang, and C. Yan, "Pyramid learnable bandpass filters for ultra-high-definition image demoiréing," *IEEE Transactions on Circuits and Systems for Video Technology*, 2025.
- [22] R. Cong, R. Liao, F. Li, R. Sheng, H. Bai, R. Wan, S. Kwong, and W. Zhang, "Reference-based iterative interaction with p 2-matching for stereo image super-resolution," *IEEE Transactions on Image Processing*, 2025.
- [23] X. Wang, M. Liu, F. Wang, J. Dai, A.-A. Liu, and Y. Wang, "Relation-preserving feature embedding for unsupervised person re-identification," *IEEE Transactions on Multimedia*, vol. 26, pp. 714–723, 2023.
- [24] X. Yang, X. Wang, L. Liu, N. Wang, and X. Gao, "Stfe: a comprehensive video-based person re-identification network based on spatio-temporal feature enhancement," *IEEE Transactions on Multimedia*, vol. 26, pp. 7237–7249, 2024.

- [25] L. Hao, Y. Hu, Y. Yue, L. Wu, H. Fu, J. Duan, and J. Liu, "Hierarchical context transformer for multi-level semantic scene understanding," *IEEE Transactions on Circuits and Systems for Video Technology*, 2024.
- [26] R. Xing, R. Cong, Y. Wu, C. Wang, Z. Tang, F. Wang, H. Wu, and S. Kwong, "Towards ancient plant seed classification: A benchmark dataset and baseline model," *arXiv preprint arXiv:2512.18247*, 2025.
- [27] S. Lian, Z. Zhang, H. Li, W. Li, L. T. Yang, S. Kwong, and R. Cong, "Diving into underwater: Segment anything model guided underwater salient instance segmentation and a large-scale dataset," *arXiv preprint arXiv:2406.06039*, 2024.
- [28] R. Cong, H. Sun, Y. Luo, and H. Fang, "Generalized few-shot segmentation for remote sensing image based on class relation mining," *Acta Aeronautica et Astronautica Sinica*, vol. 46, no. 23, 2025.
- [29] H. Fang, R. Cong, X. Lu, X. Zhou, S. Kwong, and W. Zhang, "Decoupled motion expression video segmentation," in *Proceedings of the Computer Vision and Pattern Recognition Conference*, 2025, pp. 13 821–13 831.
- [30] J. Wu, W. Zhou, X. Qian, J. Lei, L. Yu, and T. Luo, "Mfenet: Multitype fusion and enhancement network for detecting salient objects in rgb-t images," *Digital Signal Processing*, vol. 133, p. 103827, 2023.
- [31] J. Zhang, R. Zhang, L. Xu, X. Lu, Y. Yu, M. Xu, and H. Zhao, "Fastersal: Robust and real-time single-stream architecture for rgb-d salient object detection," *IEEE Transactions on Multimedia*, 2024.
- [32] G. Chen, Q. Wang, B. Dong, R. Ma, N. Liu, H. Fu, and Y. Xia, "Emtrans: Edge-aware multimodal transformer for rgb-d salient object detection," *IEEE Transactions on Neural Networks and Learning Systems*, vol. 36, no. 2, pp. 3175–3188, 2024.
- [33] R. Cong, N. Yang, H. Liu, D. Zhang, Q. Huang, S. Kwong, and W. Zhang, "Trnet: Two-tier recursion network for co-salient object detection," *IEEE Transactions on Circuits and Systems for Video Technology*, vol. 35, no. 6, pp. 5844–5857, 2025.
- [34] S. Ma, K. Song, H. Dong, H. Tian, and Y. Yan, "Modal complementary fusion network for rgb-t salient object detection," *Applied Intelligence*, vol. 53, no. 8, pp. 9038–9055, 2023.
- [35] C. Lv, X. Zhou, B. Wan, S. Wang, Y. Sun, J. Zhang, and C. Yan, "Transformer-based cross-modal integration network for rgb-t salient object detection," *IEEE Transactions on Consumer Electronics*, 2024.
- [36] H. Zhou, C. Tian, Z. Zhang, C. Li, Y. Xie, and Z. Li, "Frequency-aware feature aggregation network with dual-task consistency for rgb-t salient object detection," *Pattern Recognition*, vol. 146, p. 110043, 2024.
- [37] Z. Liu, Y. Tan, Q. He, and Y. Xiao, "Swinnet: Swin transformer drives edge-aware rgb-d and rgb-t salient object detection," *IEEE Transactions on Circuits and Systems for Video Technology*, 2021.
- [38] C. Li, J. Guo, B. Wang, R. Cong, Y. Zhang, and J. Wang, "Single underwater image enhancement based on color cast removal and visibility restoration," *Journal of Electronic Imaging*, vol. 25, no. 3, pp. 033 012–033 012, 2016.
- [39] M. Feng, H. Lu, and E. Ding, "Attentive feedback network for boundary-aware salient object detection," in *Proceedings of the IEEE/CVF Conference on Computer Vision and Pattern Recognition*, 2019, pp. 1623–1632.
- [40] Q. Zhang, R. Cong, C. Li, M.-M. Cheng, Y. Fang, X. Cao, Y. Zhao, and S. Kwong, "Dense attention fluid network for salient object detection in optical remote sensing images," *IEEE Transactions on Image Processing*, vol. 30, pp. 1305–1317, 2020.
- [41] Y. Wang, K. Song, J. Liu, H. Dong, Y. Yan, and P. Jiang, "Renet: Rectangular convolution pyramid and edge enhancement network for salient object detection of pavement cracks," *Measurement*, vol. 170, p. 108698, 2021.
- [42] M. Ma, C. Xia, C. Xie, X. Chen, and J. Li, "Boosting broader receptive fields for salient object detection," *IEEE Transactions on Image Processing*, 2023.
- [43] L. Zhang and Q. Zhang, "Salient object detection with edge-guided learning and specific aggregation," *IEEE Transactions on Circuits and Systems for Video Technology*, vol. 34, no. 1, pp. 534–548, 2023.
- [44] Z. Wang, Y. Zhang, Y. Liu, D. Zhu, S. A. Coleman, and D. Kerr, "Elwnet: An extremely lightweight approach for real-time salient object detection," *IEEE Transactions on Circuits and Systems for Video Technology*, vol. 33, no. 11, pp. 6404–6417, 2023.
- [45] R. Yan, L. Yan, G. Geng, Y. Cao, P. Zhou, and Y. Meng, "Asnet: Adaptive semantic network based on transformer-cnn for salient object detection in optical remote sensing images," *IEEE Transactions on Geoscience and Remote Sensing*, 2024.
- [46] N. Huang, Q. Jiao, Q. Zhang, and J. Han, "Middle-level feature fusion for lightweight rgb-d salient object detection," *IEEE Transactions on Image Processing*, vol. 31, pp. 6621–6634, 2022.
- [47] M. Song, W. Song, G. Yang, and C. Chen, "Improving rgb-d salient object detection via modality-aware decoder," *IEEE Transactions on Image Processing*, vol. 31, pp. 6124–6138, 2022.
- [48] X. Fang, M. Jiang, J. Zhu, X. Shao, and H. Wang, "Grouptransnet: Group transformer network for rgb-d salient object detection," *Neurocomputing*, vol. 594, p. 127865, 2024.
- [49] Z. Feng, W. Wang, W. Li, G. Li, M. Li, and M. Zhou, "Mfur-net: Multimodal feature fusion and unimodal feature refinement for rgb-d salient object detection," *Knowledge-Based Systems*, p. 112022, 2024.
- [50] G. Chen, F. Shao, X. Chai, H. Chen, Q. Jiang, X. Meng, and Y.-S. Ho, "Cgmdrnet: Cross-guided modality difference reduction network for rgb-t salient object detection," *IEEE Transactions on Circuits and Systems for Video Technology*, vol. 32, no. 9, pp. 6308–6323, 2022.
- [51] H. He, J. Wang, X. Li, M. Hong, S. Huang, and T. Zhou, "Eaf-net: an enhancement and aggregation-feedback network for rgb-t salient object detection," *Machine Vision and Applications*, vol. 33, no. 4, p. 64, 2022.
- [52] J. Wang, G. Li, H. Yu, J. Xi, J. Shi, and X. Wu, "Intra-modality self-enhancement mirror network for rgb-t salient object detection," *IEEE Transactions on Circuits and Systems for Video Technology*, 2024.
- [53] H. Yue, J. Guo, X. Yin, Y. Zhang, and S. Zheng, "Salient object detection in low-light rgb-t scene via spatial-frequency cues mining," *Neural Networks*, vol. 178, p. 106406, 2024.
- [54] J. He, K. Fu, X. Liu, and Q. Zhao, "Samba: A unified mamba-based framework for general salient object detection," in *Proceedings of the Computer Vision and Pattern Recognition Conference*, 2025, pp. 25 314–25 324.
- [55] Z. Liu, X. Wang, X. Fang, Z. Tu, and L. Wang, "Samsod: Rethinking sam optimization for rgb-t salient object detection," *IEEE Transactions on Multimedia*, 2026.
- [56] P.-T. De Boer, D. P. Kroese, S. Mannor, and R. Y. Rubinstein, "A tutorial on the cross-entropy method," *Annals of operations research*, vol. 134, no. 1, pp. 19–67, 2005.
- [57] M. A. Rahman and Y. Wang, "Optimizing intersection-over-union in deep neural networks for image segmentation," in *International symposium on visual computing*. Springer, 2016, pp. 234–244.
- [58] K. Zhao, S. Gao, W. Wang, and M.-M. Cheng, "Optimizing the f-measure for threshold-free salient object detection," in *Proceedings of the IEEE/CVF International Conference on Computer Vision*, 2019, pp. 8849–8857.
- [59] Z. Tu, Z. Li, C. Li, Y. Lang, and J. Tang, "Multi-interactive dual-decoder for rgb-thermal salient object detection," *IEEE Transactions on Image Processing*, vol. 30, pp. 5678–5691, 2021.
- [60] W. Gao, G. Liao, S. Ma, G. Li, Y. Liang, and W. Lin, "Unified information fusion network for multi-modal rgb-d and rgb-t salient object detection," *IEEE Transactions on Circuits and Systems for Video Technology*, 2021.
- [61] F. Huo, X. Zhu, L. Zhang, Q. Liu, and Y. Shu, "Efficient context-guided stacked refinement network for rgb-t salient object detection," *IEEE Transactions on Circuits and Systems for Video Technology*, vol. 32, no. 5, pp. 3111–3124, 2021.
- [62] W. Zhou, Q. Guo, J. Lei, L. Yu, and J.-N. Hwang, "Eccfnnet: Effective and consistent feature fusion network for rgb-t salient object detection," *IEEE Transactions on Circuits and Systems for Video Technology*, 2021.
- [63] W. Zhou, Y. Zhu, J. Lei, J. Wan, and L. Yu, "Apnet: Adversarial learning assistance and perceived importance fusion network for all-day rgb-t salient object detection," *IEEE Transactions on Emerging Topics in Computational Intelligence*, vol. 6, no. 4, pp. 957–968, 2021.
- [64] J. Wang, K. Song, Y. Bao, L. Huang, and Y. Yan, "Cgfnnet: Cross-guided fusion network for rgb-t salient object detection," *IEEE Transactions on Circuits and Systems for Video Technology*, vol. 32, no. 5, pp. 2949–2961, 2021.
- [65] Z. Tu, Y. Ma, Z. Li, C. Li, J. Xu, and Y. Liu, "Rgbd salient object detection: A large-scale dataset and benchmark," *IEEE Transactions on Multimedia*, 2022.
- [66] R. Cong, K. Zhang, C. Zhang, F. Zheng, Y. Zhao, Q. Huang, and S. Kwong, "Does thermal really always matter for rgb-t salient object detection?" *IEEE Transactions on Multimedia*, 2022.
- [67] G. Liao, W. Gao, G. Li, J. Wang, and S. Kwong, "Cross-collaborative fusion-encoder network for robust rgb-thermal salient object detection," *IEEE Transactions on Circuits and Systems for Video Technology*, vol. 32, no. 11, pp. 7646–7661, 2022.
- [68] B. Tang, Z. Liu, Y. Tan, and Q. He, "Hrtransnet: Hrformer-driven two-modality salient object detection," *IEEE Transactions on Circuits and Systems for Video Technology*, 2022.
- [69] J. Wang, K. Song, Y. Bao, Y. Yan, and Y. Han, "Unidirectional rgb-t salient object detection with intertwined driving of encoding and fusion,"

- Engineering Applications of Artificial Intelligence*, vol. 114, p. 105162, 2022.
- [70] H. Wang, K. Song, L. Huang, H. Wen, and Y. Yan, "Thermal images-aware guided early fusion network for cross-illumination rgb-t salient object detection," *Engineering Applications of Artificial Intelligence*, vol. 118, p. 105640, 2023.
- [71] Y. Pang, X. Zhao, L. Zhang, and H. Lu, "Caver: Cross-modal view-mixed transformer for bi-modal salient object detection," *IEEE Transactions on Image Processing*, vol. 32, pp. 892–904, 2023.
- [72] W. Zhou, F. Sun, Q. Jiang, R. Cong, and J.-N. Hwang, "Wavenet: Wavelet network with knowledge distillation for rgb-t salient object detection," *IEEE Transactions on Image Processing*, vol. 32, pp. 3027–3039, 2023.
- [73] Z. Zhang, J. Wang, and Y. Han, "Saliency prototype for rgb-d and rgb-t salient object detection," in *Proceedings of the 31st ACM International Conference on Multimedia*, 2023, pp. 3696–3705.
- [74] Y. Wu, T. Jia, X. Chang, H. Wang, and D. Chen, "Rgb-t saliency detection based on multi-scale modal reasoning interaction," *IEEE Transactions on Instrumentation and Measurement*, 2024.
- [75] M. Jiang, J. Ma, J. Chen, Y. Wang, and X. Fang, "Patnet: Patch-to-pixel attention-aware transformer network for rgb-d and rgb-t salient object detection," *Knowledge-Based Systems*, vol. 291, p. 111597, 2024.
- [76] K. Wang, Z. Tu, C. Li, C. Zhang, and B. Luo, "Learning adaptive fusion bank for multi-modal salient object detection," *IEEE Transactions on Circuits and Systems for Video Technology*, vol. 34, no. 8, pp. 7344–7358, 2024.
- [77] P. Lyu, P.-H. Yeung, X. Yu, C. Wu, and J. C. Rajapakse, "Deep fourier-embedded network for rgb and thermal salient object detection," *arXiv preprint arXiv:2411.18409*, 2024.
- [78] H. Tang, Z. Li, D. Zhang, S. He, and J. Tang, "Divide-and-conquer: Confluent triple-flow network for rgb-t salient object detection," *IEEE Transactions on Pattern Analysis and Machine Intelligence*, 2024.
- [79] X. Yu, X. Cheng, Y. Liu, and Z. Zheng, "A dual-stream cross-domain integration network for rgb-t salient object detection," *IEEE Transactions on Consumer Electronics*, 2024.
- [80] G. Xiao, X. Liu, Z. Lin, and R. Ming, "Smr-net: Semantic-guided mutually reinforcing network for cross-modal image fusion and salient object detection," in *Proceedings of the AAAI Conference on Artificial Intelligence*, vol. 39, no. 8, 2025, pp. 8637–8645.
- [81] Z. Tu, T. Xia, C. Li, X. Wang, Y. Ma, and J. Tang, "Rgb-t image saliency detection via collaborative graph learning," *IEEE Transactions on Multimedia*, vol. 22, no. 1, pp. 160–173, 2019.
- [82] G. Wang, C. Li, Y. Ma, A. Zheng, J. Tang, and B. Luo, "Rgb-t saliency detection benchmark: Dataset, baselines, analysis and a novel approach," in *Chinese Conference on Image and Graphics Technologies*. Springer, 2018, pp. 359–369.
- [83] J. Deng, W. Dong, R. Socher, L.-J. Li, K. Li, and L. Fei-Fei, "Imagenet: A large-scale hierarchical image database," in *2009 IEEE Conference on Computer Vision and Pattern Recognition*. Ieee, 2009, pp. 248–255.
- [84] T. Tieleman and G. Hinton, "Rmsprop: Divide the gradient by a running average of its recent magnitude. coursera: Neural networks for machine learning," *COURSERA Neural Networks Mach. Learn*, 2012.
- [85] F. Perazzi, P. Krähenbühl, Y. Pritch, and A. Hornung, "Saliency filters: Contrast based filtering for salient region detection," in *2012 IEEE/CVF Conference on Computer Vision and Pattern Recognition*, 2012, pp. 733–740.
- [86] R. Achanta, S. Hemami, F. Estrada, and S. Susstrunk, "Frequency-tuned salient region detection," in *2009 IEEE/CVF Conference on Computer Vision and Pattern Recognition*, 2009, pp. 1597–1604.
- [87] D.-P. Fan, C. Gong, Y. Cao, B. Ren, M.-M. Cheng, and A. Borji, "Enhanced-alignment measure for binary foreground map evaluation," *arXiv preprint arXiv:1805.10421*, 2018.
- [88] D.-P. Fan, M.-M. Cheng, Y. Liu, T. Li, and A. Borji, "Structure-measure: A new way to evaluate foreground maps," in *Proceedings of the IEEE/CVF International Conference on Computer Vision*, 2017, pp. 4548–4557.
- [89] K. He, X. Zhang, S. Ren, and J. Sun, "Deep residual learning for image recognition," in *Proceedings of the IEEE/CVF Conference on Computer Vision and Pattern Recognition*, 2016, pp. 770–778.